Inorganic Chemistry

Article

pubs.acs.org/IC

Preparation of Tunable (BaSrMg)O for Oxygen Chemisorption: Formation Mechanism and Characterization

Xuncai Chen,[†] Taesung Jung,[‡] Jongho Park,*[,‡] and Woo-Sik Kim*[,†]

[†]Department of Chemical Engineering, Functional Crystallization Center, Kyung Hee University, Yoing-si Kiheung-ku Seochun-dong, Seoul, Kyungki-do 449-701, Republic of Korea

[‡]Korea Institute of Energy Research, 71-2, Jangdong, Yuseong-gu, Daejeon, Republic of Korea

Supporting Information

ABSTRACT: Composition-tunable single-phase three-component alkaline earth oxide of (BaSrMg)O was prepared based on the consecutive precipitation and thermal decomposition of (BaSrMg)CO_3. First, the single-phase (BaSrMg)CO_3 was coprecipitated via ion self-assembly, phase-transformation, and agglomeration. The element composition of (BaSrMg)CO_3 could be simply tuned by the composition of the reactants. Then, (BaSrMg)CO_3 was converted to (BaSrMg)O under an H_2 atmosphere at 750 °C. This (BaSrMg)O showed fast chemisorption−desorption responses with oxygen chemisorption rate: t_{80} = 3.9 min and desorption rate: t_{80} = 14 min and a high thermal stability for the redox reaction of BaO−BaO_2. In addition, the chemisorption capacity of (BaSrMg)O (4.39% Sr composition) is ∼1.92 mmol/g, which is much higher than the chemisorption capacity of BaO/MgO at 1.75 mmol/g (Jin et al., *Ind. Eng. Chem. Res.*, **2005**, 44, 2942), while the transient oxygen pressure for the redox reaction of (BaSrMg)O (4.39% Sr composition) was significantly enhanced from 76 to 135 mmHg due to the inclusion of Sr in (BaSrMg)O. The transient oxygen pressure could be further improved via adjusting the Sr composition in (BaSrMg)O. Consequently, the tunable (BaSrMg)O has a high potential as a chemisorbent for the industrial application of oxygen separation.

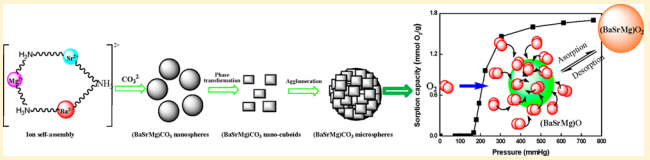

INTRODUCTION

With the increasing demand for pure oxygen in various industrial fields, such as glass melting, semiconductor manufacturing, food processing, metallurgical manufacturing, cutting and welding, fuel combustion, GTL conversion, and wastewater treatment, massive oxygen separation has become a notable challenge for new technology.[1,2]

Cryogenic distillation and physisorption are presently the most popular industrial methods for air separation.[3] Yet, while cryogenic distillation is advantageous for a large-scale air separation process, it involves high energy consumption, capital, and operating costs.[4] Similarly, while physisorption is easily commercialized, it has a poor selectivity for air separation as the physisorption enthalpies of oxygen and nitrogen are very similar.[5−7] As an alternative, oxygen-selective chemisorption has been attracting attention in recent studies, where chemisorbents, such as Co-based metal−organic host materials[7−11] and BaO-based alkaline earth oxides,[12−16] are used for the selective lattice binding of oxygen by sorption and then the reversible release of oxygen by desorption. For practical applications, BaO-based alkaline earth oxides are favored, as Co-based metal−organic frameworks include the toxic cobalt element and require a large amount of organic material, making them environmentally unfriendly. Moreover, the synthetic route for a Co-based metal−organic framework is quite complicated and includes many reaction steps. Therefore, BaO-based alkaline earth oxides are regarded as the most promising oxygen-selective chemisorbents for air separation. Notwithstanding, since BaO is very reactive, it reacts easily with its surroundings and is also sintered at an elevated temperature in the BaO-BaO_2 redox reaction, resulting in a poor thermal stability and poor productivity for a multicyclic operation. Furthermore, the transition of the BaO−BaO_2 redox reaction occurs at a low oxygen pressure, which requires a high operating cost for creating a near-vacuum condition for the release of oxygen from the BaO_2 crystals. Here, the transient oxygen pressure means the oxygen pressure required for the equilibrium of the redox reaction, and in another word that the oxidation reaction (chemisorption) proceeds at an oxygen pressure above the equilibrium pressure, while reduction (desorption) prevails at an oxygen pressure below the equilibrium pressure. As a solution to the weak points of BaO chemisorbents, additives are frequently used for the thermal stabilization of BaO and promotion of the BaO-BaO_2 redox reaction.[12,14] For example, Jin et al.[12] and Park et al.[13] used MgO powder to improve the thermal stability of the BaO−BaO_2 redox reaction at high temperature and thereby also promote the redox reaction rate. Yet, this method does not ensure the local sintering of BaO due to the nonuniform mixture of the MgO and BaO powders. Plus, the low transient oxygen pressure of the BaO−BaO_2 redox reaction remains unsolved. As a result, single-phase multicomponent alkaline oxides, such as (BaSrMg)O, were developed and investigated in our recent study as oxygen-selective chemisorbents for practical application.[16] Incorporating Mg into a (BaSrMg)O lattice was

Received: February 25, 2015
Published: May 12, 2015

ACS Publications © 2015 American Chemical Society

DOI: 10.1021/acs.inorgchem.5b00454
Inorg. Chem. 2015, 54, 5419−5425

found to improve the thermal stability of BaO and sustain the lattice structure of (BaSrMg)O even at a high temperature over 700 °C. Meanwhile, incorporating Sr enhances the transient oxygen pressure of the BaO−BaO_2 redox reaction, resulting in significant cost-savings. However, in our previous study, the synthetic method does not allow any tuning of the alkaline earth components of (BaSrMg)O, because (BaSrMg)CO_3, which is the precursor of (BaSrMg)O, is always recrystallized to the most stable phase in the composition of Ba^{2+} = 0.52, Sr^{2+} = 0.06, and Mg^{2+} = 0.42 during two-step synthetic route. As a result, optimizing the performance of the chemisorbent via the composition-tuning of (BaSrMg)O is impossible. Moreover, the previous multistep synthetic route involves a long solid−liquid reaction time for (BaSrMg)CO_3, making it unfavorable for practical application.

Accordingly, the present study proposes a simple and composition-tunable method for single-phase three-component alkaline earth oxides of (BaSrMg)O on a practical scale. Plus, the formation mechanism of (BaSrMg)CO_3 is investigated, and the performance of (BaSrMg)O for oxygen selective chemisorption is characterized.

EXPERIMENTAL SECTION

1. Synthesis of (BaSrMg)CO_3 Microspheres. The reagents of $Ba(NO_3)_2$, $Sr(NO_3)_2$, $Mg(NO_3)_2{\cdot}6H_2O$ were all purchased from Sigma-Aldrich (ACS grade). A $Ba(NO_3)_2$ aqueous solution (100 mL, 84.8 g/L), a $Sr(NO_3)_2$ aqueous solution (100 mL, 17.1 g/L), and a $Mg(NO_3)_2$ aqueous solution (100 mL, 103.8 g/L) were mixed in a round-bottom flask equipped with a reflux condenser and heated to 90 °C using a heating mantle. Next, a $(NH_4)_2CO_3$ aqueous solution (100 mL, 155.7 g/L) was added to the above mixture of $Ba(NO_3)_2$, $Sr(NO_3)_2$, and $Mg(NO_3)_2$ for the coprecipitation of (BaSrMg)CO_3. After 4 h, The (BaMgSr)CO_3 crystals in the final suspension were removed by filtration, using a filter paper, and washed with distilled water. The filtered crystals were then dried in a convection oven at 110 °C overnight. Thereafter, the dried (BaMgSr)CO_3 crystals were calcinated in a tube furnace at 750 °C under a H_2 environment (H_2 flow rate = 100 mL/min) for 4 h to obtain (BaMgSr)O crystals.

2. Analysis of (BaSrMg)CO_3 Microspheres. The size and shape of the (BaSrMg)CO_3 crystals were examined using field emission scanning electron microscopy (FE-SEM, LEO SUPRA 55 microscope, Carl Zeiss, Germany) and field emission transmission electron microscopy (FE-TEM, using a JEM-2100F microscope operated at 200 kV). Their structure was analyzed using power X-ray diffraction (M18XHF-SRA, Mac Science) with Cu Kα radiation (λ = 1.540 56 Å) and Fourier transform (FT)-Raman spectrometer with laser wavelength of 785 nm (Renishaw Micro Raman, Renishaw). The solid product compositions of (BaMgSr)CO_3 samples were analyzed using inductively coupled plasma (ICP, Direct Reading Echelle ICP, Leeman) and energy-dispersive spectrometry (EDS) element mapping (Oxford INCA Resolution 30 mm^2 136 eV at Mn Kα 5 B to 92 U). The thermogravimetric analyzer (SDTQ600, TA) was used to exam the decomposition behavior of the (BaMgSr)CO_3 crystals.

3. O_2 Chemisorption/Desorption. A thermogravimetric analyzer (SDTQ600, TA) was used to determine the sorption capacity of the (BaSrMg)O chemisorbent. The (BaSrMg)O sample (~50 mg) was placed in the TGA chamber and heated to 700 °C at 5 K/min. After stabilizing the temperature at 700 °C, a (1 atm) gas mixture (O_2 and N_2 gas) was injected into the TGA chamber. Here, the oxygen partial pressure was controlled from 80−760 mmHg using mass flow controllers (5850E, Brooks). The pressures of N_2 and O_2 were monitored using a flow and pressure controller (GMC 1200, ISVT). Every 1 h, the oxygen and nitrogen partial pressure was changed for the sorption/desorption isotherm. Here, the total gas pressure was always fixed at 760 mmHg.

4. Analysis Using Isotope of $^{18}O_2$. The chemisorption mechanism was studied using an oxygen isotope ($^{18}O_2$). The (BaSrMg)O sample was placed on a hot stage (700 °C) under vacuum conditions, and $^{18}O_2$ gas was slowly injected onto the hot stage (Linkam TS 1500, Linkam Scientific Instrument) up to 1 atm. After 3 h, the sample was cooled to room temperature and analyzed as regards the chemisorption of $^{18}O_2$ in the sample using an FT-Raman spectrometer and laser wavelength of 785 nm (Renishaw Micro Raman, Renishaw).

RESULTS AND DISCUSSION

The element compositions (Ba, Sr, and Mg) of the single-phase (BaSrMg)CO_3 (BSMC) particles prepared using the proposed synthetic method are summarized in Table 1. The experimental results show that the Ba, Sr, and Mg compositions in the BSMC particles were finely tuned according to the reactant composition without a phase separation. In addition, the EDS mapping (Supporting Information, Figure S1) revealed that BSMC samples were uniformly composed of Ba, Sr, and Mg. Also, the EDS element analysis (Supporting Information, Figure S2) confirmed that the Ba, Sr, and Mg compositions in the BSMC particles were tunable, which matched well with the average particle composition analyzed using ICP (Table 1). Plus, the Sr composition was also controllable from 4.39% to 25.64%, indicating that the proposed method can provide a higher adjustability of the transient oxygen pressure for the redox reaction when compared with the previous synthetic method.[16]

Table 1. Reactant Composition for Co-Precipitation of (BaSrMg)CO_3 and Element Compositions of (BaSrMg)CO_3 Products

	reactant composition			solid product composition		
samples[a]	$[Ba^{2+}]$ %	$[Sr^{2+}]$ %	$[Mg^{2+}]$ %	Ba %	Sr %	Mg %
$BSMC^{I}$	45	5	50	45.96	4.39	49.65
$BSMC^{II}$	40	10	50	40.84	9.36	49.80
$BSMC^{III}$	35	15	50	35.79	13.85	50.36
$BSMC^{IV}$	30	20	50	31.02	19.09	50.05
$BSMC^{V}$	25	25	50	25.64	24.03	50.33

[a]Note: all the samples were obtained with the reaction time of 4 h at 90 °C in 1.62 mol/L $(NH)_2CO_3$ solution.

The structure and shape of the BSMC particles were analyzed using powder pattern XRD, Raman spectroscopy, and SEM, as shown in Figures 1 and 2. The X-ray diffraction (XRD) patterns in Figure 1 reveal that the BSMC structures were commonly based on a main plane of (104), regardless of the element composition. Thus, the characteristic peaks of the XRD patterns were similar for all the BSMCs. When compared with the JCPDS data (12−0530) for (BaMg)CO_3, the crystal frame of (BaMg)CO_3 (BMC) was also seemingly the backbone structure of the BSMCs, and the Ba^{2+} in the crystals was replaced by Sr^{2+} to generate single-phase BSMC particles. Thus, the characteristic peaks of the BSMCs were almost identical to those of BMC, yet their positions were slightly shifted to a higher angle due to the lattice constriction as the Sr composition in the BSMC increased (from $BSMC^{I}$ to $BSMC^{V}$). That is, as the Ba^{2+} in the BSMC was replaced with Sr^{2+}, the distance between the crystal planes was reduced as the ionic radius (1.6 Å) of Ba^{2+} is larger than that of Sr^{2+} (1.44 Å),[17] resulting in a peak position shift to a higher angle. This result was also reflected in the crystal lattice parameters of the BSMCs, calculated based on a least-squares analysis of the X-ray diffraction data. The crystal lattice parameters of $BSMC^{I}$,

DOI: 10.1021/acs.inorgchem.5b00454
Inorg. Chem. 2015, 54, 5419−5425

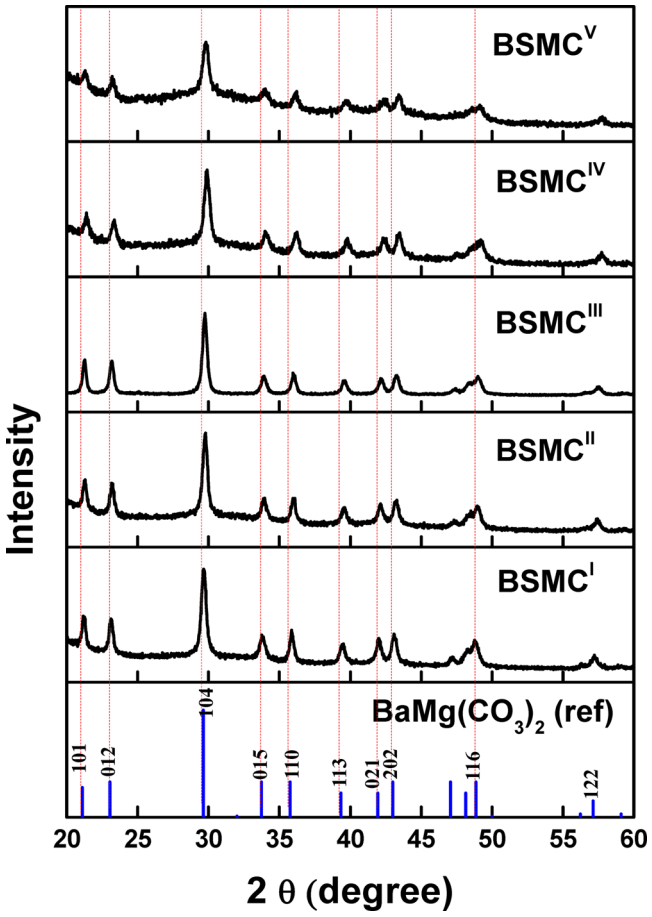

Figure 1. X-ray powder patterns of BSMC samples and comparison with reference data of $BaMg(CO_3)_2$ (JCPDS No. 12−0530).

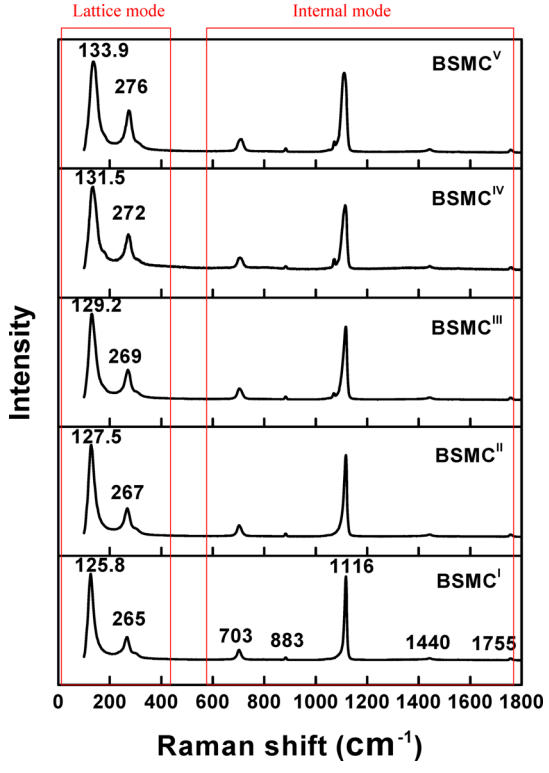

Figure 2. Raman spectrum of BSMC samples.

a = 5.0085 Å and c = 16.7189 Å, shrank to a = 4.9627 Å and c = 16.5945 Å in $BSMC^V$ when increasing the Sr composition from 4.39% to 24.03%.

According to the Raman spectra of the BSMCs shown in Figure 2, their internal modes were always observed in a band range between 700 and 1800 cm^{-1}. Thus, the bands at 883 and 1116 cm^{-1} were due to out-of-plane bending ($\upsilon 2$) and the symmetric stretch ($\upsilon 1$) of CO_3^{2-}, respectively, as similarly observed in the Raman spectrum of norsethite.[18] The band at 703 cm^{-1} was likely due to O−C−O bending ($\upsilon 4$), while the peaks at 1440 and 1755 cm^{-1} were attributed to the asymmetric stretch of the carbonate ions ($\upsilon 3$) and out-of-plane bending mode ($2{\cdot}\upsilon 3$), respectively. Here, the frequencies of the internal modes were almost independent of the Sr composition of the BSMC. However, the frequencies of the lattice modes (vibration and translation) did vary with the Sr composition in the BSMC. Thus, the vibrational and translational frequencies of $BSMC^I$ (Sr = 4.39%), occurring at 265 and 125.8 cm^{-1}, respectively, shifted to 276 and 133.9 cm^{-1}, respectively, when increasing the Sr composition to 24.03% ($BSMC^V$). This frequency shift was due to the difference in the metal bond length between Ba−O and Sr−O. That is, since the polarizability of Sr was higher than that of Ba, the metal bond length of Sr−O was shorter than that of Ba−O, which led to a blue shift of the lattice mode when increasing the Sr composition in the BSMC.[19−21] Furthermore, the metal bond length change with the metal ion replacement in the BSCM also brought about an increase in the full width at half-maximum of the Raman peaks in both the internal and lattice modes due to the partial stain in the crystal structure of BSMC.[22]

The SEM images in the Supporting Information (Figure S3) showed that the BSMC particles were spherical aggregates consisting of nanocuboids. In addition, a TGA curve (Supporting Information Figure S4) of $BSMC^{II}$ revealed two mass losses, occurring at 550−580 °C and 800−1220 °C, respectively, where the first mass loss (16.61%) at 550−580 °C was due to the thermal decomposition of $Mg^{2+}-CO_3^{2-}$ into $Mg^{2+}-O^{2-}$, while the second mass loss (16.7%) occurring across a wide temperature range of 800−1220 °C was due to the overlap decomposition of $Ba^{2+}-CO_3^{2-}$ and $Sr^{2+}-CO_3^{2-}$ into $Ba^{2+}-O^{2-}$ and $Sr^{2+}-O^{2-}$, respectively. The similarity between the two weight losses originated from the similar composition between $MgCO_3$ and $(BaSr)CO_3$ in the BSCM, as indicated in Table 1.

The synthetic mechanism of the BSMC particles was investigated using SEM, TEM, and powder pattern XRD, as shown in Figures 3 and 4. First, amorphous spherical BSMC particles (~350 nm) were precipitated until 15 s, as shown in the FE-SEM image (Figure 3a,b). The noncrystallinity of these nanospheres was easily confirmed by the XRD spectra, as shown in Figure 3f. After 60 s, crystalline nanosize cuboids began to appear (Figure 3c). Thus, a crystalline characteristic XRD peak of BSMC was detected at 2θ = 30°. After 120 s, all the amorphous nanospheres were converted to microspheres (1.6 μm) aggregated with small particles (Figure 3d). The XRD pattern confirmed that these microspheres were fully crystalline. Thereafter up to 4 h, the particle morphology and structure remained the same, except for a slight increase in size (Figure 3e,f).

On the basis of the above results, the formation mechanism of BSMC was described as follows: first, amorphous nanospheres of BSMC were precipitated and then converted to a

DOI: 10.1021/acs.inorgchem.5b00454
Inorg. Chem. 2015, 54, 5419−5425

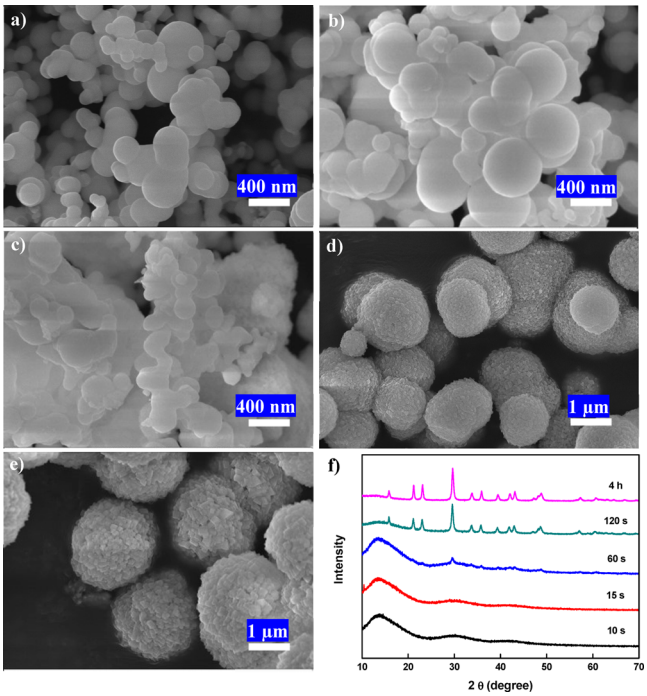

Figure 3. Transient behavior of coprecipitation of $BSMC^{II}$ at 90 °C monitored by FE-SEM and XRD: (a) products solids of $BSMC^{II}$ at 10 s, (b) products solids of $BSMC^{II}$ at 15 s, (c) products solids of $BSMC^{II}$ at 60 s, (d) products solids of $BSMC^{II}$ at 2 min, (e) products solids of $BSMC^{II}$ at 240 min. (f) XRD patterns of the corresponding products shown in (a–e).

stable phase of crystalline nanocuboids via a solvent-mediated phase transformation from unstable phase to stable phase. These nanocuboids then aggregated to form microspherical particles. This phase transformation depended on the reaction temperature, as shown in the Supporting Information (Figure S5). At a high reaction temperature of 90 °C, the amorphous nanospheres were completely converted to crystalline particles, whereas at a low reaction temperature below 60 °C, the amorphous nanospheres remained unconverted. It was due to the increase of the solubility of amorphous nanopheres with the reaction temperature, promoting the transformation of amorphous nanospheres to crystalline particles.

This mechanism was also confirmed by a TEM and EDS analysis, as shown in Figure 4. The BSMC nanospheres precipitated at 15 s did not exhibit an ordered pattern of lattice fringes (Figure 4a,b). However, the elements of Ba, Sr, and Mg were homogeneously distributed throughout the nanospheres, indicating a single-phase noncrystalline BSMC solid (Figure 4c). Meanwhile, the microspheres obtained at 4 h were aggregates of crystalline nanocuboids, as shown in the TEM image (Figure 4d) and ED pattern (Figure 4e). Plus, the EDS element mapping demonstrated single-phase BSMC particles without any phase separation.

In this precipitation, we proposed that NH_4^+ acted as a chelating agent and CO_3^{2-} served as a coprecipitating agent in the formation of the single-phase BSMC solid. The NH_4^+ and CO_3^- ions come from the dissolution of $(NH_4)_2CO_3$ in water. As described below,[23−25] Ba^{2+}, Sr^{2+}, and Mg^{2+} were simultaneously combined with NH_4^+, forming a complex of $[BaSrMg(NH_3)_n]^{2+}$. This complex was then converted to a three-component solid of $(BaSrMg)CO_3$ by reaction with CO_3^{2-}.

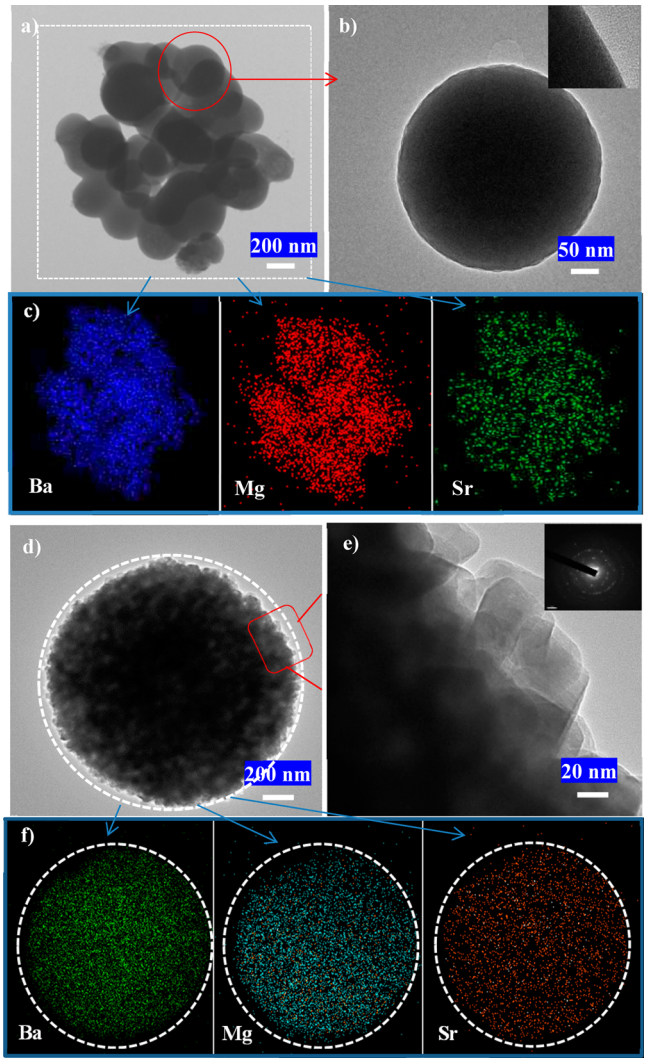

Figure 4. (a)TEM image of $BSMC^{II}$ nanospheres obtained at reaction time of 15 s; (b) TEM image of a single $BSMC^{II}$ nanosphere; (c) element mapping of Ba, Mg, and Sr in $BSMC^{II}$ nanospheres shown in (a); (d) TEM image of a single $BSMC^{II}$ microsphere obtained at reaction time of 4 h; (e) TEM mage of individual crystal composing $BSMC^{II}$ microsphere shown in (d) with SAED pattern; (f) element mapping of Ba, Mg, and Sr in $BSMC^{II}$ microsphere (d).

$$Ba^{2+}(aq) + Sr^{2+}(aq) + Mg^{2+}(aq) + nNH_4^+ + nOH^- \rightarrow [BaSrMg(NH_3)_n]^{2+}(aq) + nH_2O(aq) \quad (1)$$

$$[BaSrMg(NH_3)_n]^{2+}(aq) + CO_3^{2-} + nH_2O \rightarrow [BaSrMg]CO_3(s) + nNH_4^+ + nOH^- \quad (2)$$

Here, NH_4^+ of a chelating agent prevented a phase separation into single-component particles ($BaCO_3$, $SrCO_3$, $MgCO_3$) and double-component particles ($(BaSr)CO_3$, $(BaMg)CO_3$, $(SrMg)CO_3$). The key role of the NH_4^+ ions in the three-component coprecipitation is briefly presented in the Supporting Information (Figure S6). Thus, phase separation occurred when using Na_2CO_3 as the carbonate reactant, whereas single-phase BSMC was obtained when using NH_4^+ with Na_2CO_3.

To characterize the chemisorption, $(BaSrMg)CO_3$ ($BSMC^{II}$ and $BSMC^{IV}$) was converted to the oxide form of (BaSrMg)O ($BSMO^{II}$ and $BSMO^{IV}$, respectively) via thermal decomposi-

DOI: 10.1021/acs.inorgchem.5b00454
Inorg. Chem. 2015, 54, 5419−5425

tion under an H_2 environment at 750 °C,[26] and these BSMOs were then reacted with O_2 for oxygen chemisorption. According to the sorption isotherm of O_2 at 700 °C (Figure 5a,b), the oxygen chemisorption of $BSMO^{I}$ (4.39% Sr composition) began above an oxygen partial pressure of 135 mmHg, referred to as the transient oxygen pressure for the BaO−BaO_2 redox reaction. Plus, this transient oxygen pressure increased to 228 mmHg in the case of $BSMO^{V}$ (24.03% Sr composition). When compared with previous reported data on the transient oxygen pressures of (BaMg)O as 76 mmHg,[27] the present transient oxygen pressure (228 mmHg) was much higher due to the Sr element incorporated in the BSMO. According to de La Croix et al.,[28] the lattice energy of Sr−O (−3240 kJ/mol) is higher than that of Ba−O (−3021 kJ/mol), due to the stronger electron attraction of Sr than Ba. Therefore, this produced a relatively weaker and longer Ba−O bondage in Ba−O−Sr than the Ba−O bondage in Ba−O−Ba. Thus, the Ba−O bondage in Ba−O−Sr was more easily broken for oxidation to Ba−O−O−Sr in the oxygen chemisorption, when compared with the breakage of the Ba−O bondage in Ba−O−Ba for oxidation to Ba−O−O−Ba. Inversely, for the oxygen desorption, Ba−O−O−Sr was more easily reduced to Ba−O−Sr when compared with the reduction of Ba−O−O−Ba to Ba−O−Ba. Thus, the Ba−O−Sr and Ba−O−O−Sr were likely in equilibrium at a higher oxygen partial pressure than the Ba−O−Ba and Ba−O−O-Ba system. As a result, the equilibrium of the BSMO−$BSMO_2$ ((BaSrMg)O−(BaSrMg)O_2) redox reaction shifted to a higher oxygen partial pressure when increasing the Sr composition in the BSMO. To confirm this hypothesis, the coordination states of BSMOs were investigated using XPS analysis. Figure 6a showed the XPS spectra in the O 1s binding energy region of the BSMO samples. In all cases, an intense peak was observed at ∼530 eV, yet their positions were slightly shifted to a higher binding energy. Meanwhile, the peak width was broadened as the Sr composition in the BSMC increased (from $BSMC^{I}$ to $BSMC^{V}$). Since the bonding energy of Sr−O was higher than that of Ba−O as mentioned above, the coordination state of oxygen ions in the BSMO was changed as the Sr was incorporated in the BSMO, leading to the chemical shift of O 1s. Therefore, the change of the coordination of oxygen ions in the covalent character of M−O bonds would affect the redox reaction of BSMO. In addition, the BSMO−$BSMO_2$ redox reaction was analyzed using an isotope of oxygen ($^{18}O_2$). In the Raman spectra, the three absorption peaks for three O−Os, including $^{18}O-^{18}O$, $^{18}O-^{16}O$, and $^{16}O-^{16}O$, in $BSMO^{II}$ were slightly red-shifted from 813, 837.8, and 859 cm^{-1} to 811, 834.9, and 856 cm^{-1}, respectively, when increasing the Sr composition from 9.36% to 19.09% in the BSMO (Figure 6b). This was due to the strong Sr−O bonding, which reduced the O−O vibration energy in the Ba−O−O−Sr. In addition, the intensity ratio of the Raman bands for the labeled O−Os ($^{18}O-^{18}O/^{18}O-^{16}O/^{16}O-^{16}O$ = 2.3:1:0.3) indicated

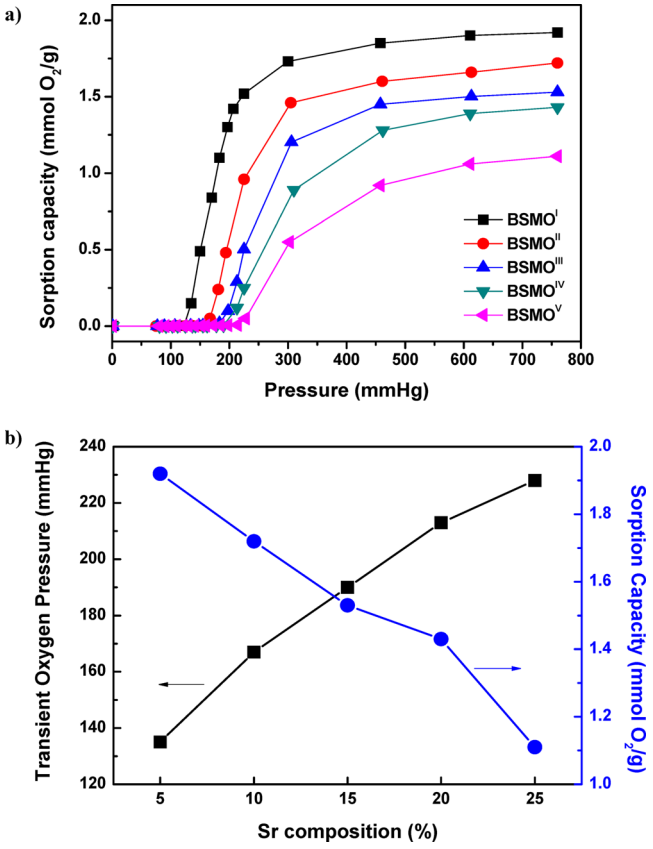

Figure 5. (a) Oxygen sorption isotherm and capacity of BSMOs ($BSMO^{I}$, $BSMO^{II}$, $BSMO^{III}$, $BSMO^{IV}$, and $BSMO^{V}$) at 700 °C measured with thermogravimetry; (b) effect of Sr composition in the BSMO on the transient oxygen pressure and sorption capacity of BSMO oxygen chemisorption.

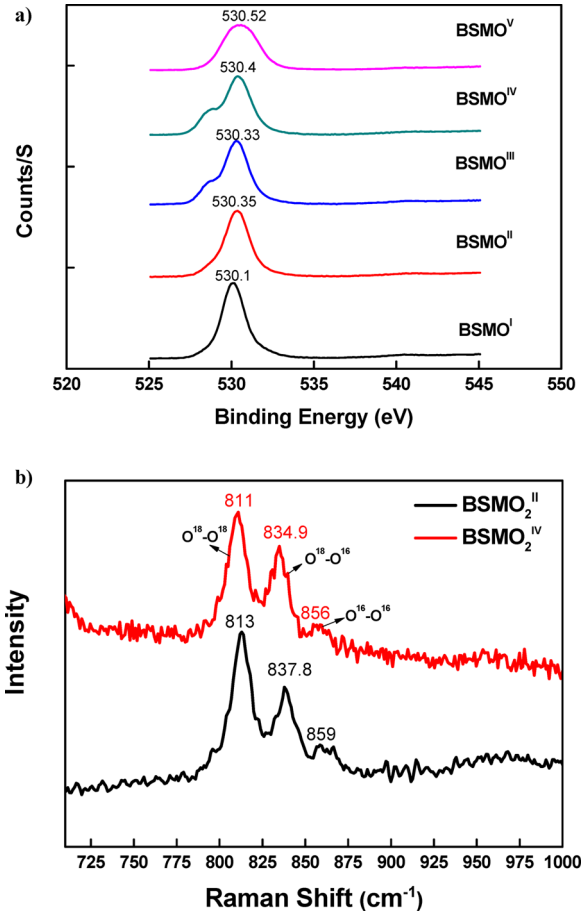

Figure 6. (a) XPS spectrum of the BSMOs ($BSMO^{I}$, $BSMO^{II}$, $BSMO^{III}$, $BSMO^{IV}$, and $BSMO^{V}$) samples: the O 1s binding energy region. (b) Raman spectra of $BSMO_2$s ($BSMO_2^{II}$ and $BSMO_2^{IV}$) after chemisorption of $^{18}O_2$ gas at 700 °C for 3 h.

DOI: 10.1021/acs.inorgchem.5b00454
Inorg. Chem. 2015, 54, 5419−5425

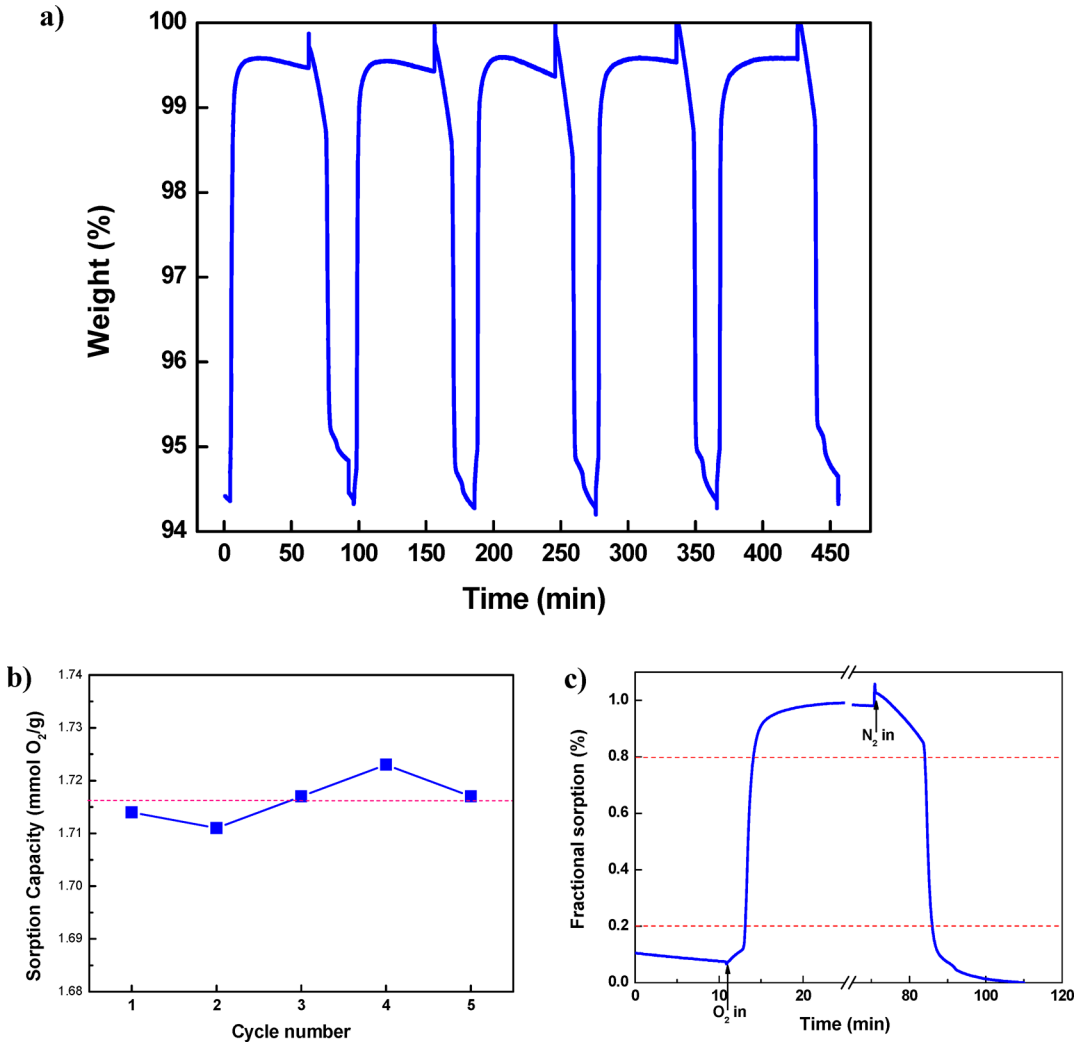

Figure 7. (a) Multicycle adsorption−desorption of O_2 on $BSMO^{II}$ crystals, (b) the oxygen sorption capacity versus cycle number for the oxygen chemisorption of $BSMO^{II}$, (c) one cycle of sorption and desorption, relaxation time, t_{80}, was measured based on 80% weight change. All analyses were measured by TGA at 700 °C.

that the BSMO easily reacted with oxygen to form $BSMO_2$. In addition, the sorption isotherm (Figure 5a) also revealed that the $BSMO^{I}$ has a much higher sorption capacity (1.92 mmol O_2/g) than that (1.75 mmol O_2/g) of (BaMg)O, as previously reported by Jin his co-workers.[12] However, the oxygen chemisorption capacity was reduced from 1.92 mmol O_2/g ($BSMO^{II}$) to 1.11 mmol O_2/g ($BSMO^{IV}$) due to the decreased Ba composition when increasing the Sr composition in the BSMO (Figure 5b).

The thermal stability and capacity reproducibility of the BSMO were tested using multiple chemisorption−desorption cycles. As shown in Figure 7a, no significant change was recorded in the chemisorption and desorption profiles over five cycles, demonstrating the high thermal stability of the sorbent due to the incorporation of Mg in the crystals. Here, the MgO in the BSMO crystals played a role of a robust barrier due to its high thermal stability. So, it inhibited the fluidization or aggregation of BaO_2 in the BSMO crystals. The oxygen sorption capacity was always ~1.716 mmol O_2/g within ±0.6% of fluctuation over five cycles, as shown Figure 7b, which revealed the good reproducibility of BSMO for the oxygen chemisorption. In addition, the BSMO exhibited fast chemisorption (t_{80} = 3.8 min), representing a much faster adsorption rate than that for (BaO_2/MgO) prepared using hydrothermal (t_{80} = 4 min) and sol−gel (t_{80} = 6−9 min) methods, as reported by Park et al.[13], and the desorption was also much faster, where the desorption time, t_{80} = 13 min, responses to the redox reaction, as shown in Figure 7c. It should be mentioned that the relaxation time, t_{80}, was defined as the time required for the fractional approach to reach 80% of the reaction from an equilibrium state to a new one, as reported by Lin et al.[14]

CONCLUSIONS

In summary, a composition-tunable method for multiple-component single-phase alkaline earth compounds of (BaSrMg)O was presented. In the co-precipitation, the element compositions of Ba, Sr, and Mg in the $(BaSrMg)CO_3$ could be easily controlled by adjusting the reactant compositions. Also, $(BaSrMg)CO_3$ microspheres were formed based on ion self-assembly, phase transformation (from amorphous nanospheres to crystalline nanocuboids), and agglomeration of the nanocuboids in an NH_4^+ aqueous medium. The $(BaSrMg)CO_3$ was easily converted to (BaSrMg)O being used for oxygen chemisorption via a redox reaction. As substituting Sr for Ba weakened the Ba−O bondage in Ba−O−Sr, the Ba−O binding

DOI: 10.1021/acs.inorgchem.5b00454
Inorg. Chem. 2015, 54, 5419−5425

was easily broken for oxidation to Ba−O−O−Sr in the oxygen chemisorption. Conversely, Ba−O−O−Sr was easily reduced to Ba−O−Sr in the oxygen desorption. Thus, the oxygen partial pressure for the transition of the (BaSrMg)O−(BaSrMg)O_2 redox reaction was significantly enhanced according to the Sr composition in (BaSrMg)O. In addition, (BaSrMg)O exhibited a high thermal stability and durability over multiple chemisorption−desorption cycles, and fast chemisorption (t_{80} = 3.8 min) and desorption (t_{80} = 13 min) responses to the redox reaction. Consequently, the composition-tunable (BaSrMg)O exhibited effective oxygen chemisorption characteristics applicable for industrial air separation. Plus, the proposed synthetic method can also be extended to the preparation of other multicomponent metal carbonates or/and oxide materials.

■ ASSOCIATED CONTENT

Ⓢ Supporting Information

EDS mapping and element analyses of Ba, Sr, and Mg, SEM images, TGA curve, FE-SEM images, XRD patterns. The Supporting Information is available free of charge on the ACS Publications website at DOI: 10.1021/acs.inorgchem.5b00454.

■ AUTHOR INFORMATION

Corresponding Authors

*E-mail: wskim@khu.ac.kr. (W.S.K.)
*E-mail: jongho@kier.re.kr. (H.J.P.)

Author Contributions

The manuscript was written based on contributions from all authors. All authors have given their approval to the final version of the manuscript.

Notes

The authors declare no competing financial interest.

■ ACKNOWLEDGMENTS

This work was conducted under the framework of the Research and Development Program of the Korea Institute of Energy Research (KIER; B4-2442-02).

■ REFERENCES

(1) Badwal, S. P. S.; Ciacchi, F. T. *Adv.Mater.* **2001**, *13*, 993−996.
(2) Watson, C. F.; Whitley, R. D.; Meyer, M. L. U.S. Patten, Patent No: US 5529610. 1996.
(3) Toftegaard, M. B.; Brix, J.; Jensen, P. A.; Glarborg, P.; Jensen, A. D. *Prog. Energy Combust. Sci.* **2010**, *36*, 581−625.
(4) Gaffney, T. R. *Curr. Opin. Solid State Mater. Sci.* **1996**, *1*, 69−75.
(5) Cengel, Y.; Boles, M. *Thermodynamics: An Engineering Approach;* Mcgraw- Hill: New York, 5th ed.; 2006.
(6) Sircar, S.; Rao, M. B.; Golden, T. C. *Adsorption and its Applications in Industry and Environmental Protection;* Elsevier Science Publ B V: Amsterdam, 1999, *120*, 395−423.
(7) Ismail, A. F.; David, L. I. B. *J. Membr. Sci.* **2001**, *193*, 1−18.
(8) Southon, P. D.; Price, D. J.; Nielsen, P. K.; McKenzie, C. J.; Kepert, C. J. *J. Am. Chem. Soc.* **2011**, *133*, 10885−10891.
(9) Zhang, D.; Stephenson, N. A. *Adsorption* **2014**, *20*, 137−146.
(10) Hutson, N. D.; Yang, R. T. *Ind. Eng. Chem. Res.* **2000**, *39*, 2252−2259.
(11) Ramprasad, D.; Pez, G. P.; Pearlstein, R. M.; Meier, I. K. US Patent, Patent No: US 5126466. 1992.
(12) Jin, C.; Hirose, T.; Koto, M. *Ind. Eng. Chem. Res.* **2005**, *44*, 2942−2947.
(13) Park, J. H.; Cho, Y. S.; Yi, K. B.; Han, S. S.; Cho, S. H. *Appl. Surf. Sci.* **2010**, *256*, 5528−5532.
(14) Jin, C.; Suehiro, T.; Kodama, A.; Goto, M.; Hirose, T. *J. Chem. Eng. Jpn.* **2001**, *34*, 279−282.
(15) Park, J. H. WO patent, Patent No: 2012102554A3, 2012.
(16) Chen, X. C.; Tung, T. S.; Park, J. H.; Kim, W. S. *J. Mater. Chem. A* **2015**, *3*, 258−265.
(17) Chen, Y. H.; Yu, S. C.; Huang, E.; Lee, P. L. *Phys. B* **2010**, *405*, 4386−4388.
(18) Scheetz, B. E.; White, W. B. *Am. Mineral.* **1977**, *62*, 36−50.
(19) Wang, D. B.; Hamm, L. M.; Bodnar, R. J.; Dove, P. M. *J. Raman Spectrosc.* **2012**, *43*, 543−548.
(20) Bischoff, W. D.; Sharma, S. K.; Macenzie, F. T. *Am. Mineral.* **1985**, *70*, 581−589.
(21) Booker, M. H.; Bredig, M. A. *J. Chem. Phys.* **1973**, *58*, 5319−5321.
(22) Lin, F.; Sum, A. K.; Bodnar, R. J. *J. Raman Spectrosc.* **2007**, *38*, 1510−1515.
(23) Park, S. H.; Shin, H. S.; Myung, S. T.; Yoon, C. S.; Amine, K.; Sun, Y. K. *Chem. Mater.* **2005**, *17*, 6−8.
(24) Lee, M. H.; Kang, Y. J.; Myung, S. T.; Sun, Y. K. *Electrochim. Acta* **2004**, *50*, 939−948.
(25) Sun, Y. K.; Chen, Z. H.; Noh, H. J.; Lee, D. J.; Jung, H. G.; Ren, Y.; Wang, S.; Yoon, C. S.; Myung, S. T.; Amine, K. *Nat. Mater.* **2012**, *11*, 942−947.
(26) Reller, A.; Padeste, C.; Hug, P. *Nature* **1987**, *329*, 527−529.
(27) Mestl, G.; Rosynek, M. P.; Lunsford, J. H. *J. Phys. Chem. B* **1998**, *102*, 154−161.
(28) De La Croix, A.; English, R. B.; Brow, M. E. *J. Solid State Chem.* **1998**, *137*, 346−352.

DOI: 10.1021/acs.inorgchem.5b00454
Inorg. Chem. 2015, 54, 5419−5425